Journal of Nuclear Materials 511 (2018) 428–437

Contents lists available at ScienceDirect

Journal of Nuclear Materials

journal homepage: www.elsevier.com/locate/jnucmat

Synergistic effects of Ln and Fe Co-Doping on phase evolution of $Ca_{1-x}Ln_xZrTi_{2-x}Fe_xO_7$ (Ln = La, Nd, Gd, Ho, Yb) ceramics

Shiyin Ji [a, b], Yuhong Li [a], Shengshou Ma [b, c], Chengshuai Liu [e], Kaimin Shih [d], Chang-Zhong Liao [b, d, *]

[a] School of Nuclear Science and Technology, Lanzhou University, Lanzhou, 730000, China
[b] Guangdong Key Laboratory of Integrated Agro-environmental Pollution Control and Management, Guangdong Institute of Eco-environmental Science & Technology, Guangzhou, 510650, China
[c] College of Resources, Environment and Materials, Guangxi University, Nanning, 530004, China
[d] Department of Civil Engineering, The University of Hong Kong, Hong Kong Special Administrative Region
[e] State Key Laboratory of Environmental Geochemistry, Institute of Geochemistry, Chinese Academy of Sciences, Guiyang, 550081, China

HIGHLIGHTS

- Single zirconolite phase cannot form in the $Ca_{1-x}La_xZr_2Ti_{2-x}Fe_xO_7$ solid solutions.
- Both zirconolite-2M and 3O can be observed in the Nd-Fe and Gd-Fe co-doped samples.
- Complete solid solution of $Ca_{1-x}(Ho/Yb)_xZr_2Ti_{2-x}Fe_xO_7$ as zirconolite-2M cannot form.
- The variation trends in the lattice parameters of $Ca_{1-x}Ln_xZr_2Ti_{2-x}Fe_xO_7$ are different.

ARTICLE INFO

Article history:
Received 1 June 2018
Received in revised form
19 September 2018
Accepted 20 September 2018
Available online 21 September 2018

Keywords:
Zirconolite
Nuclear waste
Phase transformations
Solid solutions

ABSTRACT

Zirconolite ($CaZrTi_2O_7$) is one of the host ceramic waste forms for actinides immobilization. In this study, lanthanides were used as the surrogates for actinides and a series of solid solutions ($Ca_{1-x}Ln_xZrTi_{2-x}Fe_xO_7$; Ln = La, Nd, Gd, Ho, Yb) have been successfully fabricated to investigate the synergistic effects of Ln and Fe co-doping on phase evolution and solubility of Ln in zirconolite. Results show that zirconolite was found to co-exist with perovskite in the range $0.1 \leq x \leq 0.7$ while zirconia, pseudobrookite, and perovskite become the major crystalline phases at $0.8 \leq x \leq 1.0$ in the $Ca_{1-x}La_xZrTi_{2-x}Fe_xO_7$ ceramics. Both of zirconolite-2M and Zirconolite-3O were found in the $Ca_{1-x}Nd_xZrTi_{2-x}Fe_xO_7$ and $Ca_{1-x}Gd_xZrTi_{2-x}Fe_xO_7$ solid solutions. The phase transformation of zirconolite-2M to 3O occurs at $x = 0.6$ for $Ca_{1-x}Nd_xZrTi_{2-x}Fe_xO_7$ when this phenomenon happens at $x = 0.9$ for $Ca_{1-x}Gd_xZrTi_{2-x}Fe_xO_7$. The solubility of $Ca_{1-x}Ho_xZrTi_{2-x}Fe_xO_7$ to form single zirconolite-2M structure can be up to 0.9. Single zirconolite-2M was only detected within $0.1 \leq x \leq 0.6$ in the $Ca_{1-x}Yb_xZrTi_{2-x}Fe_xO_7$ solid solutions. Lattice parameters of zirconolite-2M and zirconolite-3O were determined by Pawley refinement method. The lattice parameters of both zirconolite 2M and 3O gradually increase with increasing Nd and Fe contents in the $Ca_{1-x}Nd_xZrTi_{2-x}Fe_xO_7$ ceramics. For $Ca_{1-x}Gd_xZrTi_{2-x}Fe_xO_7$, the lattice parameter *a* has an increase with *x* increasing while *b* and *c* change slightly. For the Ho-Fe co-doped zirconolite-2M, the lattice parameter *a* shows an increasing trend, *b* and *c* demonstrate reverse trend when increasing Ho and Fe concentrations. Both *b* and *c* decrease with *x* increasing from 0.1 to 0.6 in the $Ca_{1-x}Yb_xZrTi_{2-x}Fe_xO_7$ while *a* has a slight change. The variation trends in the lattice parameters of zirconolite-2M phase in $Ca_{1-x}REE_xZrTi_{2-x}Fe_xO_7$ (REE = Nd, Gd, Ho, Yb) solid solutions are different, and such results may suggest different substitution mechanisms of lanthanide ions and Fe^{3+} in zirconolite.

© 2018 Elsevier B.V. All rights reserved.

1. Introduction

A key factor to hinder the development of nuclear power is the safe disposal of high-level radioactive waste (HLW) from spent fuel

* Corresponding author. Department of Civil Engineering, The University of Hong Kong, Hong Kong Special Administrative Region.
E-mail address: liaocz29@connect.hku.hk (C.-Z. Liao).

https://doi.org/10.1016/j.jnucmat.2018.09.043
0022-3115/© 2018 Elsevier B.V. All rights reserved.

which contains long half-life and high radiotoxicity of radionuclides, such as U, Pu, Np, Am, Cm [1,2]. One strategy for safely disposing HLW is to immobilize them into a durable nuclear waste form and subsequently bury in the deep ground to isolate from the ecological system. Up to now, there are many nuclear waste forms in the study which can be classified into three types: glasses, glass-ceramics and ceramics [3]. Ceramic waste forms have significant advantages for actinides immobilization due to their excellent performances in waste loading and long-term durability [4–6]. In the ceramic waste forms, radionuclides can be incorporated into a durable crystalline phase at the atomic scale. Many of such crystalline phases have been studied in the past decades, such as pyrochlore, zirconolite, zircon, monazite, and apatite [7]. Zirconolite is considered as a promising candidate for immobilizing actinides nuclear waste because of its highly chemical durability, thermodynamic stability and radiation tolerance [6,8–11]. In natural zirconolite, it is found to accommodate rare-earth elements, Th, U in Ca and Zr cation site, and Al^{3+}, Fe^{3+} or other transition metals in Ti cation site for charge balance [12–14]. In addition, zirconolite is one of the major phases to incorporate long-lived radioactive actinides in SYNROC which was first proposed as a crystalline ceramic material for HLW immobilization by Ringwood in the 1970s [15].

Zirconolite (simplified formula $CaZrTi_2O_7$) is usually a two-layer monoclinic crystalline (space group C 12/c1) referred as zirconolite-2M, one layer is composed of Ca-Zr (CaO_8 and ZrO_7) plane, the other one is stacked by Ti-O polyhedra (TiO_6 and TiO_5) [16], as shown Fig. 1. Depending on the compositions and nature of substitutions, other four zirconolite polytypes were also reported in the literature: zirconolite-3O (orthorhombic polytype) [12,13], zirconolite-3T (trigonal polytype) [12,14,17], zirconolite-4M (four-layer monoclinic polytype) [17,18], and zirconolite-6T (trigonal polytype) [19]. Zirconolite-6T was only reported as an intergrowth in zirconolite-2M and 3T crystal [19]. Zirconolite-4M occurs between end-member of zirconolite-2M and pyrochlore when loading high level of rare earth elements [18,20,21]. Both zirconolite-3T and 3O are three-layered polytypes and generally appear when $CaZrTi_2O_7$ is co-doped with lanthanides (or actinides) and Fe^{3+} (or Al^{3+}) ions [17,22–24]. Zirconolite-2M has been intensively studied for minor actinides immobilization and previous studies revealed that the optimal sintering temperature to form single zirconolite-2Mphaseis at 1300-1450 °C [20,21,23,25–27].

As one of the promising host matrices for HLW immobilization, zirconolite has been investigated to incorporate Pu, U and minor actinide elements [22,28–30]. Results showed that the incorporation of U into zirconolite is approximately 0.4 formula units (f.u.) and 0.15–0.17 f.u. for Pu and Np. When co-doping with Al, the incorporation of U and Np can be increased to 0.3–0.4 f.u. and 0.4 f.u. Kesson and co-workers [31] had tested the solubility of UO_2, ThO_2 and rare earth oxides in the zirconolite structure and found the solubility of these dopants in the zirconolite structure is significantly different. Due to the radiotoxicity of actinides, many studies on the incorporation of actinides in zirconolite were performed by using non-radioactive lanthanides as surrogates with their similar charge and ionic radii [22,26,32–34]. In the $Ca_{1-x}Nd_{2x}Zr_{1-x}Ti_2O_7$ solid solution, nearly single zirconolite-2M was only observed at $x \leq 0.05$ and the single zirconolite-4M phase was detected in a range of $0.2 \leq x \leq 0.4$ [20]. Similar results were also reported in the $Ca_{1-x}REE_{2x}Zr_{1-x}Ti_2O_7$ (REE = Sm, Y) solid solutions [21,35]. In general, Al^{3+} and Fe^{3+} were used as charge compensator when incorporating trivalent (or tetravalent) lanthanides (or actinides) ions into zirconolite structure [23,24,28,33]. Previous studies revealed that almost single zirconolite-2M was obtained in the $Ca_{1-x}Nd_xZrTi_{2-x}Al_xO_7$ solid solution with $x \leq 0.65$ while single zirconolite-3O appeared at $0.7 \leq x \leq 0.85$ [23,28]. As indicated in previous studies [12–14], Fe^{3+} is one of the charge compensators to replace some Ti^{4+} for maintaining charge balance when substituting lanthanides and actinides ions into Ca^{2+} in the zirconolite in nature. Also, Fe may play an important role in corrosion in the HLW and needs to be considered in the immobilization matrix for HLW. However, limited studies were carried out to use Fe^{3+} as a charge-balancing agent in the zirconolite structure. Gilbert and co-workers [24] pointed out that the incorporation of Pu in zirconolite can be up to 0.4 f.u. in the $(Ca_{1-x}Pu_x)Zr(Ti_{2-2x}Fe_{2x})O_7$ solid solution. These results indicate that using charge compensator (such as Al^{3+} and Fe^{3+}) can enhance the solubility of lanthanides (or actinides) in zirconolite. To our knowledge, no systematic investigation was carried out to observe the co-doping Fe and lanthanides (with various ionic radii) in zirconolite structure.

Limited studies were carried out to use Fe^{3+} as a charge-balancing agent in the zirconolite structure. Gilbert and co-workers [24] pointed out that the incorporation of Pu in zirconolite can be up to 0.4 f.u. in the $(Ca_{1-x}Pu_x)Zr(Ti_{2-2x}Fe_{2x})O_7$ solid solution. These results indicate that using charge compensator (such as Al^{3+} and Fe^{3+}) can enhance the solubility of lanthanides (or actinides) in zirconolite. However, no study to perform a systematic work on co-doping Fe and lanthanides with various ionic radii in zirconolite structure was investigated.

In this study, nonradioactive trivalent lanthanides were proposed to incorporate into Ca^{2+} site in zirconolite with Fe^{3+} substituting Ti^{4+} for charge equilibrium. A series of samples with $Ca_{1-x}Ln_xZrTi_{2-x}Fe_xO_7$ ($Ln = La, Nd, Gd, Ho, Yb$; $0.1 \leq x \leq 1$) were prepared by high-temperature solid-state reaction. The aim is to systematically investigate the phase evolution and solubility in

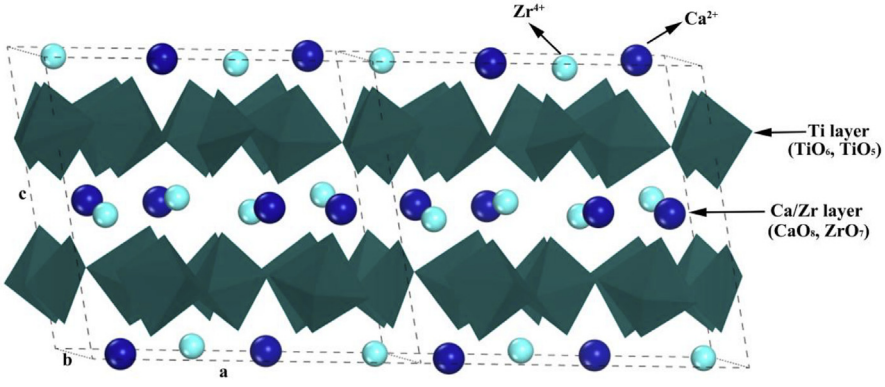

Fig. 1. Schematic representation of the two-layered zirconolite (zirconolite-2M).

zirconolite when co-doping Fe and lanthanides with different ionic radii. Powder X-ray diffraction (XRD), scanning electron microscopy (SEM) and energy dispersive X-Ray spectroscopy (EDX) were employed to characterize the products. In addition, the lattice parameters of zirconolite phase were determined by using Pawley refinement method based on the XRD patterns [36].

2. Experimental procedures

Series of compositions with stoichiometry $Ca_{1-x}Ln_xZrTi_{2-x}Fe_xO_7$ (Ln = La, Nd, Gd, Ho, Yb; $0.1 \le x \le 1$) were fabricated by high-temperature solid-state reaction. The raw materials (purity≥99.9%) are $CaCO_3$, ZrO_2, TiO_2, Fe_2O_3, La_2O_3, Nd_2O_3, Gd_2O_3, Ho_2O_3 and Yb_2O_3. Stoichiometric amounts of raw materials were thoroughly homogenized using agate mortar and then pressed into 12 mm diameter pellets. Braeden et al. [27] had tested the effects of sintering temperature and time on the formation of $CaCe_xZr_{1-x}Ti_2O_7$ zirconolite and found that single zirconolite phase can be obtained when sintering condition is at 1350 °C for 24 h. Therefore, all the pellets were sintered at 1400 °C for 50 h in our study, except those of $Ca_{1-x}La_xZrTi_{2-x}Fe_xO_7$ ($0.1 \le x \le 1$). Our pre-experiment showed that the $Ca_{1-x}La_xZrTi_{2-x}Fe_xO_7$samples melted when sintering at 1400 °C. Thus, the $Ca_{1-x}La_xZrTi_{2-x}Fe_xO_7$ samples were sintered at 1300 °C for 50 h. In order to obtain homogenous samples, the pellets were reground into powder, pressed into pellets and sintered at 1400 °C (or 1300 °C) for 50 h again.

The products were ground into fine powder for powder X-ray diffraction (XRD) analysis. All the powder XRD patterns are recorded on a Bruker D8 Advance diffractometer equipped with Cu Kα source (40 kV, 40 mA) and LynxEye detector. The 2θ scanning range was 10–110° and the step size was 0.02° with a scanning speed of 1s step^{-1}. The crystalline phases were qualitatively identified by matching the powder XRD patterns with equivalent patterns retrieved from the standard powder diffraction database of the International Centre for Diffraction Data (ICDD PDF-2, RELEASE 2008). The lattice parameters were determined by using GSASII software with Pawley refinement method [37]. The obtained specimens were also ground and polished for SEM characterization. A Hitachi S-3400N SEM equipped with an EDX elemental microanalysis system was used to investigate the morphology and chemical compositions.

3. Results and discussion

3.1. Multiple phases in $Ca_{1-x}La_xZrTi_{2-x}Fe_xO_7$ solid solutions

The phase compositions of the $Ca_{1-x}La_xZrTi_{2-x}Fe_xO_7$ ($x = 0.1$–0.5) samples are shown in Fig. 2a. Both zirconolite-2M and perovskite crystalline phases were observed, indicating that single phase of zirconolite-2M cannot form in the nominal compositions with $0.1 \le x \le 0.5$. It is noticed that the perovskite phase was indexed to be cubic rather than orthorhombic or monoclinic [38]. As shown in Fig. 2b, the back-scattered SEM image of $Ca_{0.5}La_{0.5}ZrTi_{1.5}Fe_{0.5}O_7$ also confirms the existence of two crystalline phases, in which the grey matrix corresponds to zirconolite-2M where the white areas refer to the perovskite grain. In addition, the intensity of the characteristic peak ($2\theta = 32.8°$) of perovskite phases increases when dopant concentration from $x = 0.1$ to 0.5, suggesting the increasing fractions of perovskite in the samples.

For the nominal $x = 0.6$ sample, four crystalline phases such as zirconolite-2M, zirconolite-3O, monoclinic zirconia and cubic perovskite were detected in its XRD pattern, as shown in Fig. 3a. Notably, only three contrasts were observed in the back-scattered SEM image of this sample, as shown in Fig. 3b. This phenomenon seems not consistent with the XRD result. Further investigation by EDX analysis indicates that there are two distinguishable spectra for the white grains, as shown in Fig. 3d and e. Quantitative EDX analysis shows that the "1 site" spectrum relates to the zirconia phase where the "2 site" spectrum refers to the perovskite phase. The elemental mapping was utilized to determine the spatial distribution of Zr also clearly reveal the difference of chemical compositions in these white grains (Fig. 3f).

At the nominal composition with $x = 0.7$, the characteristic peak ($2\theta = 31.8°$) of zirconolite-2M disappear, and peaks of orthorhombic pseudobrookite (Fe_2TiO_5) were observed (Fig. 3a). Consequently, the $Ca_{0.3}La_{0.7}ZrTi_{1.3}Fe_{0.7}O_7$ sample consists of four crystalline phases, zirconolite-3O, cubic perovskite, monoclinic zirconia and pseudobrookite (Fe_2TiO_5). Similar to the case of the $x = 0.6$ sample, only three contrasts were observed in the back-scattered SEM image of $Ca_{0.3}La_{0.7}ZrTi_{1.3}Fe_{0.7}O_7$ (Fig. 3c), in which the dark and grey grains are corresponding to pseudobrookite and zirconolite-3O, respectively. EDX analysis was also performed on the white grains to distinguish zirconia and perovskite crystals. As shown in Fig. 3g and h, the "3 site" spectrum is rich in Zr corresponding to zirconia phase while the "4 site" spectrum can be attributed to perovskite.

Fig. 4a displays the XRD patterns and phase identification results of nominal $Ca_{1-x}La_xZrTi_{2-x}Fe_xO_7$ samples with $x = 0.8$–1.0. It can be seen that cubic perovskite, monoclinic zirconia, and pseudobrookite are present in these products. The cubic perovskite became the major phase and no zirconolite-type phase was observed in these three solid solutions. In Fig. 4b, the back-scattered SEM of the nominal $x = 0.8$ sample only present two contrasts in which the dark areas refer to the pseudobrookite phase. As shown in Fig. 4c and d, EDX analysis performing on the white grains reveals that there are significant differences in chemical compositions between grain "1" and grain "2", where the grain "1" is rich in Zr referring to zirconia phase and the grain "2" is

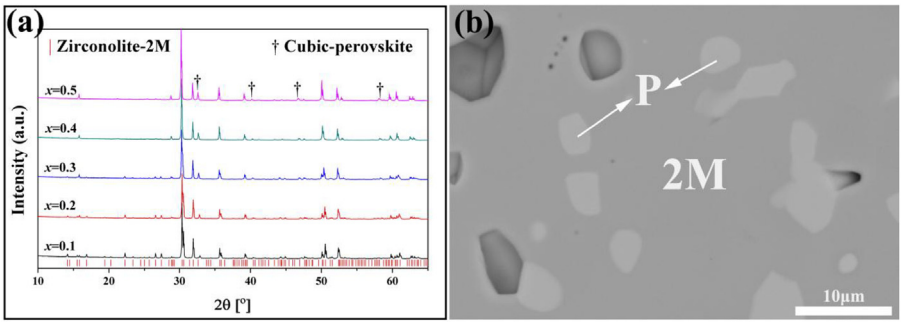

Fig. 2. XRD phase identification results of $Ca_{1-x}La_xZrTi_{2-x}Fe_xO_7$ ($x = 0.1$–0.5) samples (a), the back-scattered SEM image of the $x = 0.5$ sample (b). The grain marked "2M" is zirconolite-2M ($Ca_{0.44}La_{0.56}Zr_{1.26}Ti_{1.28}Fe_{0.46}O_7$) and the grains marked "P" are the perovskite ($Ca_{0.18}La_{0.79}Zr_{0.09}Ti_{0.74}Fe_{0.20}O_3$).

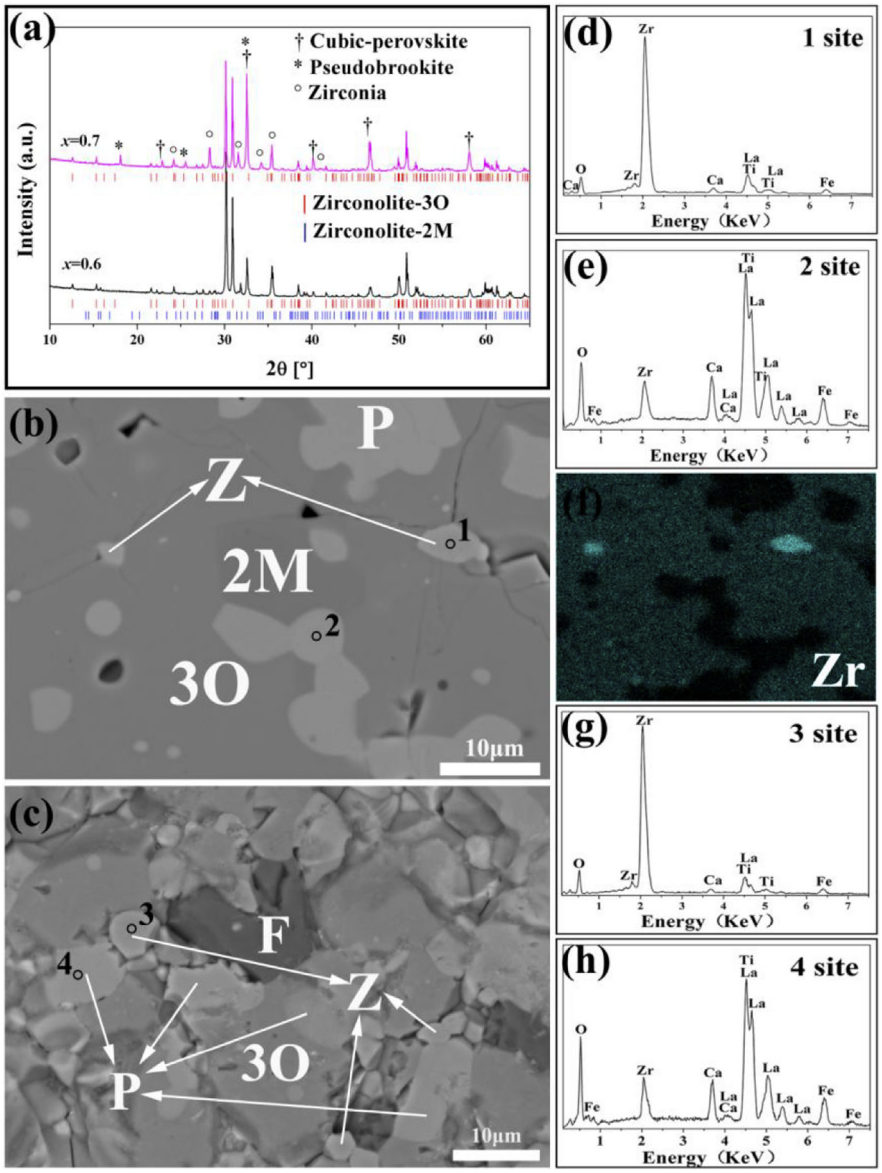

Fig. 3. XRD phase identification results of the nominal $Ca_{1-x}La_xZrTi_{2-x}Fe_xO_7$ ($x = 0.6$, 0.7) (a). Back-scattered SEM images of $x = 0.6$(b), $x = 0.7$ (c), and their corresponding EDX spectra (d), (e), (g) and (h), Elemental mapping of Zr (f). The grains marked "2M", "3O", "P", "Z" and "F" are related to zirconolite-2M ($Ca_{0.46}La_{0.49}Zr_{1.08}Ti_{1.42}Fe_{0.55}O_7$), zirconolite-3O ($x = 0.6$: $Ca_{0.39}La_{0.55}Zr_{1.07}Ti_{1.39}Fe_{0.60}O_7$; $x = 0.7$: $Ca_{0.34}La_{0.57}1Zr_{1.16}Ti_{1.30}Fe_{0.63}O_7$), perovskite ($x = 0.6$: $Ca_{0.22}La_{0.56}Zr_{0.16}Ti_{0.80}Fe_{0.26}O_3$; $x = 0.7$: $Ca_{0.19}La_{0.57}Zr_{0.19}Ti_{0.76}Fe_{0.29}O_3$), zirconia ($x = 0.6$: $Zr_{0.65}Ca_{0.04}La_{0.06}Ti_{0.18}Fe_{0.07}O_2$; $x = 0.7$: $Zr_{0.73}Ca_{0.03}La_{0.05}Ti_{0.13}Fe_{0.06}O_2$) and pseudobrookite ($Fe_{1.56}Ca_{0.06}La_{0.10}Zr_{0.27}Ti_{1.01}O_5$), respectively.

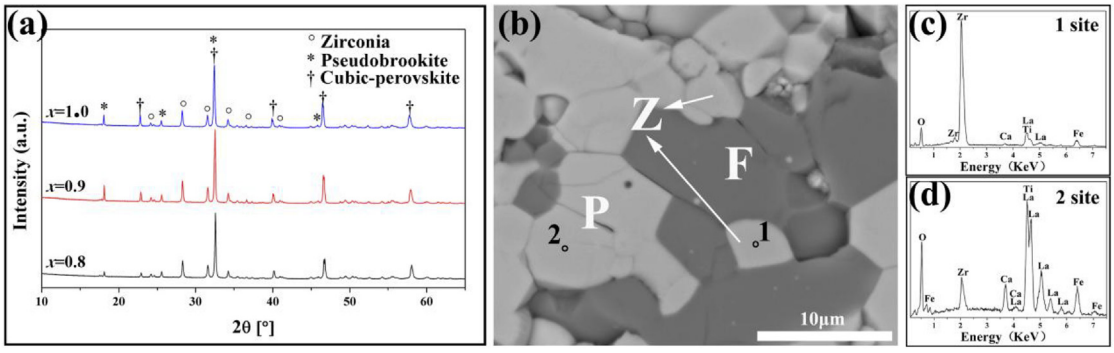

Fig. 4. XRD phase identification results of $Ca_{1-x}La_xZrTi_{2-x}Fe_xO_7$ ($x = 0.8$–1.0) (a). Back-scattered SEM image of the $x = 0.8$ sample (b), EDX spectrum of "1" (c) and "2" (d). (P: perovskite ($Ca_{0.16}La_{0.59}Zr_{0.2}Ti_{0.73}Fe_{0.32}O_3$), Z: zirconia ($Zr_{0.71}Ca_{0.02}La_{0.06}Ti_{0.13}Fe_{0.08}O_2$), F: pseudobrookite ($Fe_{1.53}Ca_{0.04}La_{0.15}Ti_{0.99}Zr_{0.29}O_5$)).

corresponding to perovskite phase. Furthermore, the difficulty in distinguishing perovskite and monoclinic zirconia grains in the back-scattered SEM images of $x = 0.6,0.7,0.8$ samples may because of the similarity of the average atomic number between perovskite $(Ca,La)(Ti,Zr,Fe)O_3$ and zirconia $(Zr,Ca,La,Ti,Fe)O_2$.

3.2. Zirconolite-2M and 3O in $Ca_{1-x}Nd_xZrTi_{2-x}Fe_xO_7$ and $Ca_{1-x}Gd_xZrTi_{2-x}Fe_xO_7$ solid solutions

As shown in Fig. 5a, the XRD patterns of the $Ca_{1-x}Nd_xZrTi_{2-x}Fe_xO_7$ samples with $0.1 \leq x \leq 0.5$ are almost indexed by zirconolite-2M structure with a trace of perovskite phase. When x increases to 0.6, an additional peak at $2\theta = 31.03°$ appears, which is the characteristic peak of zirconolite-3O (space group Acam) [13], indicating the existence of three crystalline phases in this sample. These results are similar to those in $Ca_{1-x}Nd_xZrTi_{2-x}Al_xO_7$ system reported by Loiseau and co-workers [23], in which the authors pointed out that the zirconolite-3O appears at $x = 0.65$. In addition, the back-scattered SEM images of the nominal $Ca_{0.7}Nd_{0.3}ZrTi_{1.7}Fe_{0.3}O_7$ and $Ca_{0.4}Nd_{0.6}ZrTi_{1.4}Fe_{0.6}O_7$ samples also confirm the phase identification results of their corresponding XRD patterns. In Fig. 6a, two distinguishable areas were observed, in which the grey area relates to zirconolite-2M grain while the dark area refers to perovskite grain. Fig. 6b shows three identical areas, in which the dark area refers to perovskite grain. The white area should correspond to the zirconolite-3O grain while the grey area belongs to zirconolite-2M grain. The reason is that the zirconolite-3O has a higher substitution level of Nd and Fe than zirconolite-2M, resulting in a higher average atomic number in zirconolite-3O. The XRD patterns of compositions with $0.7 \leq x \leq 1.0$ shown in Fig. 5a demonstrate that all the reflections can be indexed by zirconolite-3O. Observation of single contrast in the back-scattered SEM image also adapts the single phase in the $NdZrTiFeO_7$ sample, as shown in Fig. 6c.

Fig. 5b shows the main characteristic peaks of zirconolite-2M or 3O in the range of $29.5° \leq 2\theta \leq 33°$. It is noticed that these peaks shift to the lower angle with the concentrations of Nd and Fe rise, indicating an increase in the lattice parameters of zirconolite-2M or 3O. According to the XRD patterns, lattice parameters of zirconolite-2M and 3O phases can be obtained by using Pawley refinement implemented in GSASII [37], as summarized in Table 1. The lattice parameters of zirconolite-2M and 3O show an increase with increasing doping level of Nd and Fe. The changes in the lattice parameters of these two crystalline phases may relate to both factors. The first one is the different sizes of the cationic radii ($r(Ca^{2+}) = 1.12$ Å in 8-coordination, $r(Ti^{4+}) = 0.605$ Å in 6-coordination and 0.51 Å in 5-coordination, $r(Zr^{4+}) = 0.78$ Å in 7-coordination, $r(Nd^{3+}) = 1.109$Å in 8-coordination, $r(Fe^{3+}) = 0.58$ Å in 5-coordination and 0.55 Å in 6-coordination) [39]. The other one is the substitution mechanism of these ions in zirconolite structure.

The XRD results of samples with compositions of $Ca_{1-x}Gd_xZrTi_{2-x}Fe_xO_7$ ($x = 0.1$–1.0) also demonstrated the existence of zirconolite-2M and 3O. In Fig. 7a, all the peaks in the XRD patterns of the samples with $x = 0.1$ to 0.8 were indexed by zirconolite-2M while those in the samples with $x = 0.9$ and 1.0 contributed to zirconolite-3O. A two-phase region consisted of zirconolite-2M and 3O cannot be observed in the investigated compositions. Fig. 7b displays an obvious peak shifting of the main peaks of zirconolite-2M and 3O within the range of $29.1° \leq 2\theta \leq 33°$, suggesting a significant change in the lattice parameters of these two phases. With the Pawley method, the lattice parameters of zirconolite-2M and 3O in the $Ca_{1-x}Gd_xZrTi_{2-x}Fe_xO_7$ ceramics were determined based on their XRD data, as summarized in Table 2. In the zirconolite-2M type structure of $Ca_{1-x}Gd_xZrTi_{2-x}Fe_xO_7$ series ($0.1 \leq x \leq 0.8$), the parameters a decreases with the increase of dopant contents (Gd and Fe) whereas there is no significant change in the lattice parameters b and c. This concentration dependence of lattice parameters in the zirconolite-2M of the $Ca_{1-x}Gd_xZrTi_{2-x}Fe_xO_7$ samples further confirm the incorporation of Gd and Fe into the zirconolite-2M structure and may relate to the substitution of Gd^{3+} ions in zirconolite structure and the radius difference among Ca^{2+}, Zr^{4+}, Ti^{4+}, Gd^{3+}, and Fe^{3+} ions. Furthermore, there are two obvious peaks ((221) and (−402) planes in the zirconolite 2M structure) around 30.5° in the $Ca_{0.9}Gd_{0.1}ZrTi_{1.9}Fe_{0.1}O_7$ (i.e. $x = 0.1$) sample in Fig. 7b. However, when x increases to 0.8, only one obvious peak is observed, due to the overlap of (221) and (−402) peaks. The change of d value in these two peaks can account for this phenomenon. According to the calculated lattice parameters in Table 2, it can demonstrate that the d value of

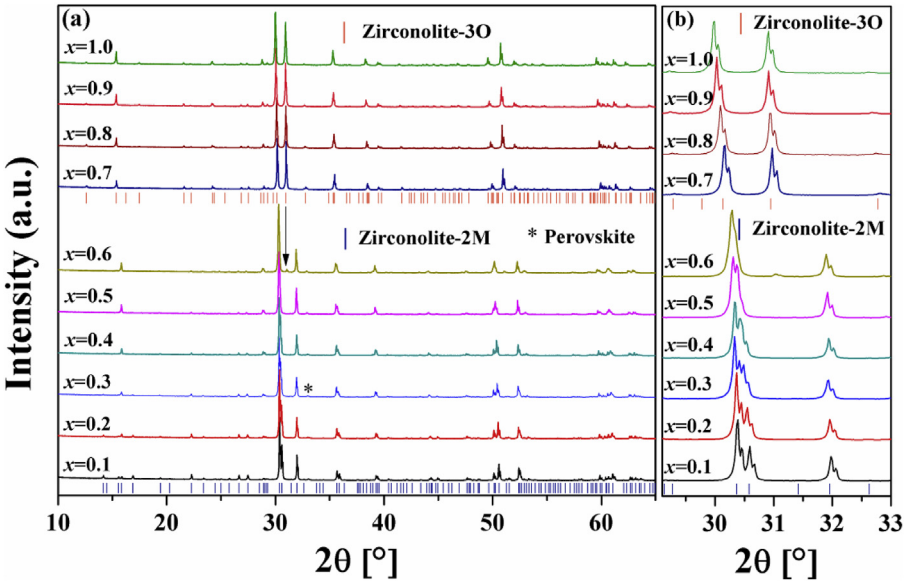

Fig. 5. Representative XRD patterns of $Ca_{1-x}Nd_xZrTi_{2-x}Fe_xO_7$ ($x = 0.1$–1.0) solid solutions (a). Details of XRD patterns among $29.5° \leq 2\theta \leq 33°$ indicated the peak shifting of zirconolite-2M and 3O (b).

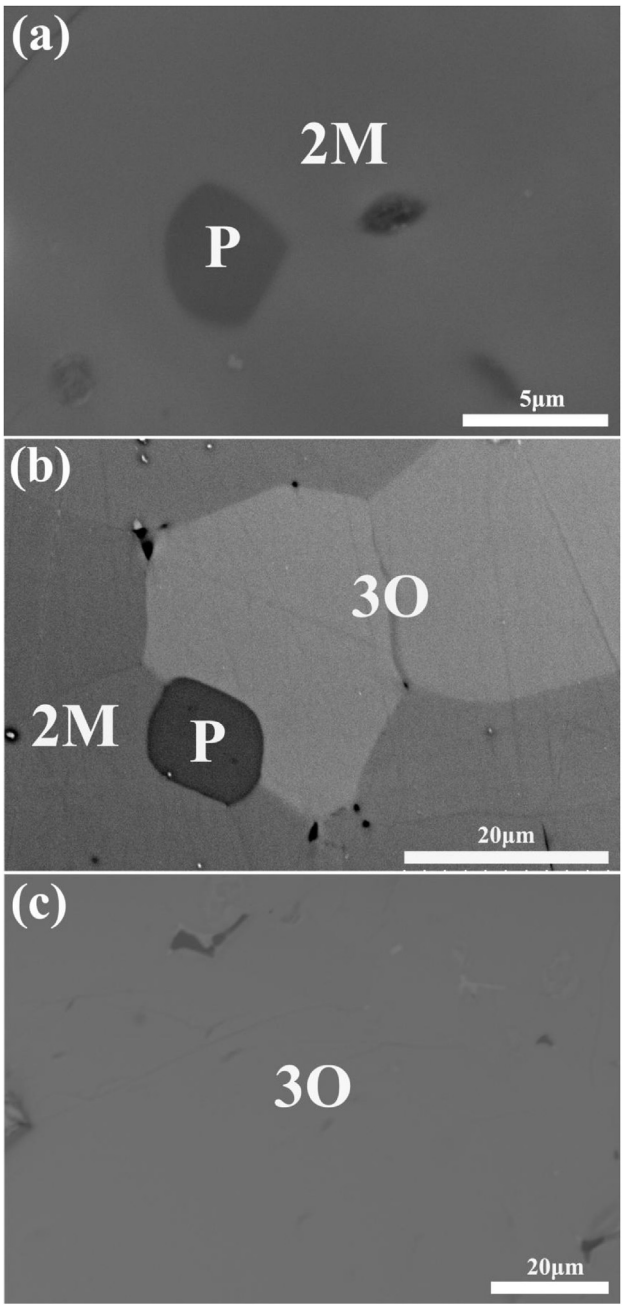

Fig. 6. Back-scattered SEM images of ceramics $x = 0.3$ (a), $x = 0.5$ (b) and $NdZrTiFeO_7$ (c). (2M: zirconolite-2M ($x = 0.3$: $Ca_{0.68}Nd_{0.28}Zr_{1.06}Ti_{1.70}Fe_{0.28}O_7$; $x = 0.6$: $Ca_{0.39}Nd_{0.58}Zr_{1.06}Ti_{1.39}Fe_{0.58}O_7$), 3O: zirconolite-3O ($x = 0.6$:$Ca_{0.33}Nd_{0.63}Zr_{1.01}Ti_{1.39}Fe_{0.64}O_7$; $x = 1.0$: $Nd_{0.98}Zr_{1.08}Ti_{1.03}Fe_{0.91}O_7$), P: perovskite ($x = 0.3$: $Ca_{0.68}Nd_{0.26}Zr_{0.02}Ti_{0.97}Fe_{0.07}O_3$; $x = 0.6$: $Ca_{0.53}Nd_{0.42}Zr_{0.01}Ti_{0.79}Fe_{0.25}O_3$)).

(221) plane is close to that of (−402) plane in the $Ca_{0.2}Gd_{0.8}ZrTi_{1.2}Fe_{0.8}O_7$ (i.e. $x = 0.8$) sample while the d values of the two peaks are largely different in the $Ca_{0.9}Gd_{0.1}ZrTi_{1.9}Fe_{0.1}O_7$ (i.e. $x = 0.1$) sample.

3.3. Solubility of $Ca_{1-x}Ho_xZrTi_{2-x}Fe_xO_7$ and $Ca_{1-x}Yb_xZrTi_{2-x}Fe_xO_7$ solid solutions

Fig. 8a displays the XRD patterns of the $Ca_{1-x}Ho_xZrTi_{2-x}Fe_xO_7$ samples in the range of $0.1 \le x \le 1.0$. Comparing the experimental XRD patterns with the standard powder diffraction of zirconolite

Table 1
Lattice parameters of zirconolite-2M and 3O in $Ca_{1-x}Nd_xZrTi_{2-x}Fe_xO_7$ solid solution.

x	Phase	a(Å)	b(Å)	c(Å)	β(°)
$x = 0.1$	2M	12.467(5)	7.277(3)	11.389(4)	100.57(1)
$x = 0.2$	2M	12.487(5)	7.279(3)	11.398(5)	100.58(1)
$x = 0.3$	2M	12.508(7)	7.281(4)	11.405(6)	100.59(1)
$x = 0.4$	2M	12.532(5)	7.285(3)	11.412(5)	100.61(1)
$x = 0.5$	2M	12.562(7)	7.288(4)	11.420(7)	100.65(1)
$x = 0.6$	2M	12.583(2)	7.289(1)	11.425(2)	100.65(1)
$x = 0.7$	3O	10.147(3)	14.044(4)	7.301(2)	90
$x = 0.8$	3O	10.158(3)	14.052(4)	7.318(2)	90
$x = 0.9$	3O	10.172(3)	14.063(4)	7.337(2)	90
$x = 1.0$	3O	10.182(3)	14.071(4)	7.357(2)	90

phase, it is noticed that almost single zirconolite-2M is observed in the samples with compositions in the range of $0.1 \le x \le 0.9$. For $x = 1.0$, although the major peaks in the XRD pattern can be indexed by zirconolite-2M (and/or 3T), there are still some differences among the weak peaks, compared with those in the sample with $x = 0.9$. As shown in Fig. 9, all the weak peaks in the XRD pattern of the sample with $x = 0.9$ can be indexed by zirconolite-2M. When x increasing to 1.0, these weak peaks cannot be observed in the XRD pattern. Instead, other weak reflections were detected in the sample with $x = 1.0$ which cannot be assigned to zirconolite-2M and may belong to an unknown phase. Thus, there are at least two crystalline phases in the sample with $x = 1.0$, i.e., zirconolite-2M (or 3T) and an unknown phase. Furthermore, the positions of the main peaks (221) and (−402) of zirconolite-2M vary when changing x from 0.1 to 0.9 (Fig. 8b), indicating that the lattice parameters change in the dependence of dopants concentration. Table 3 summaries the lattice parameters of zirconolite-2M in the $Ca_{1-x}Ho_xZrTi_{2-x}Fe_xO_7$ ($x = 0.1$–0.9) samples. Results show that the parameter a has a significant increase with increasing dopants content to $x = 0.9$ whereas the parameter b gradually decreases from $x = 0.1$ to $x = 0.6$ and then change slightly in the range $0.6 \le x \le 0.9$. There is no significant change in the lattice parameter c.

The XRD patterns of the samples with nominal compositions $Ca_{1-x}Yb_xZrTi_{2-x}Fe_xO_7$ ($x = 0.1$–1.0) are shown in Fig. 10a. The major peaks of these XRD patterns are similar to each other. However, there are some differences between the weak peaks in the ranges of $12° \le 2\theta \le 31.4°$ and $38.5° \le 2\theta \le 51°$ in the samples with $0.6 \le x \le 1.0$, as shown in Fig. 11. Results from XRD pattern indexing and Pawley fitting reveal that only all peaks in the XRD patterns of the samples in the range $0.1 \le x \le 0.6$ can be indexed by zirconolite-2M. Although the major peaks of the XRD patterns of the samples with $0.7 \le x \le 1.0$ can be indexed by zirconolite-2M, there are some weak additional reflections which cannot be assigned to zirconolite-2M, as marked by rectangles with dotted line in Fig. 11. These results may indicate that at least two crystalline phases (zirconolite-2M and an unknown phase) exist in the compositional range of $0.7 \le x \le 1.0$. Further structural investigation is needed to explain these XRD results. With considering zirconolite-2M as the main crystalline phase in the $Ca_{1-x}Yb_xZrTi_{2-x}Fe_xO_7$ ($x = 0.1$–1.0) samples, the lattice parameters were determined by Pawley refinement and were summarized in Table 4. The changes of lattice parameters with increasing the dopants concentrations in all samples indicate the continuous incorporation of Yb and Fe in the zirconolite-2M phase. In addition, the parameters a and c change slightly when the parameter b gradually decreases with increasing x from 0.1 to 1.0. The reason for such changes may relate to the substitutions of Yb^{3+}into Ca^{2+}/Zr^{4+} sites and Fe^{3+} into Ti^{4+} in zirconolite, which radii show substantial differences when they coordinated with different numbers of oxygen atoms ($r(Ca^{2+}) = 1.12$ Å in 8-coordination, $r(Ti^{4+}) = 0.605$ Å in 6-coordination and 0.51 Å in 5-coordination, $r(Zr^{4+}) = 0.78$ Å in 7-coordination,

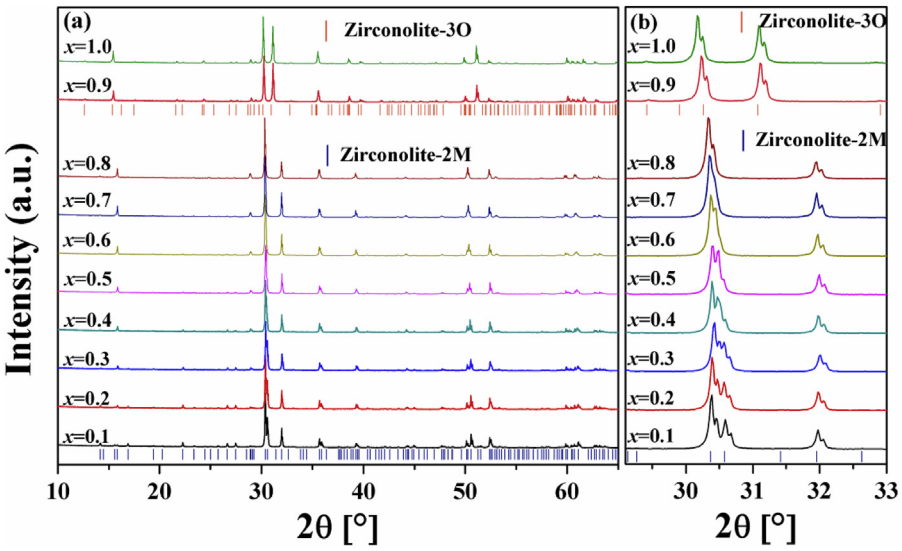

Fig. 7. Representative XRD patterns of $Ca_{1-x}Gd_xZrTi_{2-x}Fe_xO_7$ ($x = 0.1–1.0$) solid solution (a). Details of XRD patterns among $29.1° \leq 2\theta \leq 33°$ indicated the peak shifting of zirconolite-2M and 3O (b).

Table 2
Lattice parameters of zirconolite-2M and 3O in $Ca_{1-x}Gd_xZrTi_{2-x}Fe_xO_7$ solid solution.

x	Phase	a(Å)	b(Å)	c(Å)	β(°)
$x = 0.1$	2M	12.462(2)	7.275(1)	11.387(2)	100.57(1)
$x = 0.2$	2M	12.471(6)	7.270(3)	11.386(5)	100.57(1)
$x = 0.3$	2M	12.487(6)	7.268(4)	11.390(6)	100.58(1)
$x = 0.4$	2M	12.495(7)	7.268(5)	11.388(7)	100.64(1)
$x = 0.5$	2M	12.517(8)	7.267(5)	11.392(6)	100.61(1)
$x = 0.6$	2M	12.535(6)	7.267(4)	11.397(5)	100.65(1)
$x = 0.7$	2M	12.550(8)	7.268(5)	11.398(7)	100.68(2)
$x = 0.8$	2M	12.563(9)	7.271(6)	11.401(8)	100.71(2)
$x = 0.9$	3O	10.107(1)	13.985(1)	7.294(1)	90
$x = 1.0$	3O	10.110(5)	13.981(6)	7.305(3)	90

$r(Yb^{3+}) = 0.925$ Å in 7-coordination and 0.985 Å in 8-coordination, $r(Fe^{3+}) = 0.58$ Å in 5-coordination and 0.55 Å in 6-coordination) [39].

4. Conclusion

In this work, a series of Ln-Fe co-doped $Ca_{1-x}Ln_xZrTi_{2-x}Fe_xO_7$ (Ln = La, Nd, Gd, Ho, Yb) ceramics were successfully synthesized to investigate the effect of incorporating different ionic radii of lanthanides on the formation and evolution of zirconolite structure with co-doping Fe. In the La and Fe co-doping $Ca_{1-x}La_xZrTi_{2-x}Fe_xO_7$ samples, although zirconolite phase (2M or 3O) was found in the compositional range of $0.1 \leq x \leq 0.7$, other crystalline phases, such as perovskite, pseudobrookite, and zirconia, were also precipitated. For $0.8 \leq x \leq 1.0$, zirconolite cannot be observed and the major phases become zirconia, pseudobrookite, and perovskite in the La-Fe co-doped ceramics. In both $Ca_{1-x}Nd_xZrTi_{2-x}Fe_xO_7$ and $Ca_{1-x}Gd_xZrTi_{2-x}Fe_xO_7$ solid solutions, only zirconolite phase (2M or 3O) was observed in the studied range of $0.1 \leq x \leq 1.0$. A phase transformation of zirconolite-2M to zirconolite-3O was detected at

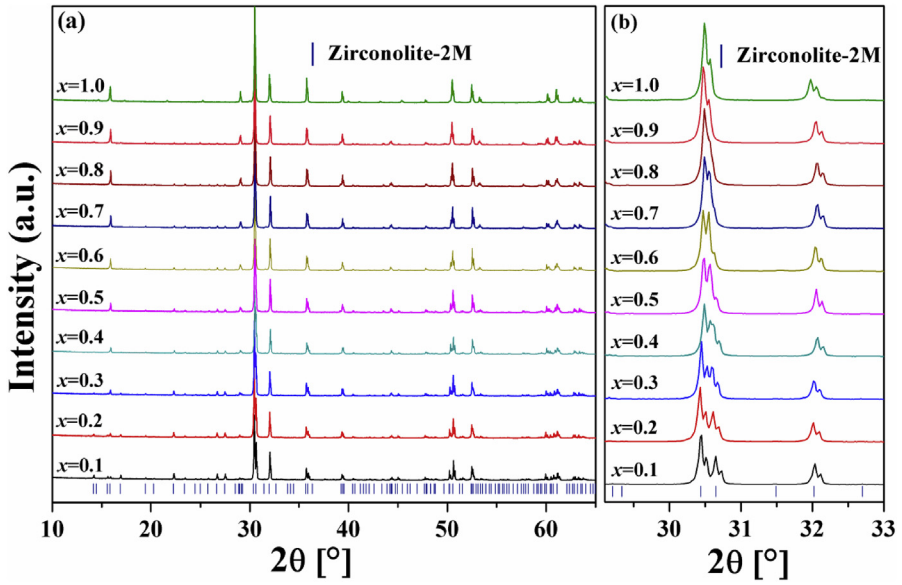

Fig. 8. Representative XRD patterns of $Ca_{1-x}Ho_xZrTi_{2-x}Fe_xO_7$ ($x = 0.1–1.0$) samples (a). Details of XRD patterns among $29.1° \leq 2\theta \leq 33°$ indicated the peak shifting of zirconolite-2M (b).

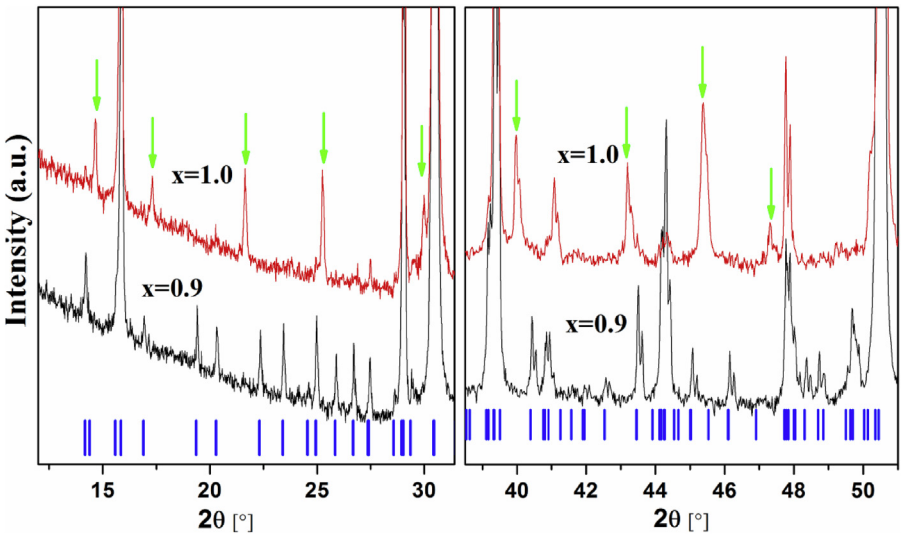

Fig. 9. Detailed XRD patterns of $Ca_{1-x}Ho_xZrTi_{2-x}Fe_xO_7$ ($x = 0.9$ and 1.0) samples in the ranges of $12° \leq 2\theta \leq 31.4°$ and $38.5° \leq 2\theta \leq 51°$. The arrows with green color indicate the additional reflections of $HoZrTiFeO_7$ sample. (For interpretation of the references to color in this figure legend, the reader is referred to the Web version of this article.)

Table 3
Lattice parameters of zirconolite-2M in $Ca_{1-x}Ho_xZrTi_{2-x}Fe_xO_7$ solid solution.

x	Phase	a(Å)	b(Å)	c(Å)	β(°)
$x = 0.1$	2M	12.455(4)	7.269(3)	11.380(4)	100.56(1)
$x = 0.2$	2M	12.460(5)	7.263(3)	11.379(5)	100.57(1)
$x = 0.3$	2M	12.466(5)	7.257(3)	11.376(5)	100.57(1)
$x = 0.4$	2M	12.473(6)	7.251(4)	11.371(5)	100.57(1)
$x = 0.5$	2M	12.481(4)	7.247(2)	11.370(3)	100.60(1)
$x = 0.6$	2M	12.487(5)	7.244(3)	11.369(5)	100.61(1)
$x = 0.7$	2M	12.498(6)	7.244(4)	11.372(5)	100.63(1)
$x = 0.8$	2M	12.506(4)	7.244(3)	11.371(4)	100.66(1)
$x = 0.9$	2M	12.514(5)	7.244(3)	11.374(5)	100.68(1)

$x = 0.6$ for Nd-Fe co-doped series while this phenomenon occurs at $x = 0.9$ for Gd-Fe co-doped samples. These results may indicate ionic radius play an important role in the formation of zirconolite-2M or 3O. For the $Ca_{1-x}Ho_xZrTi_{2-x}Fe_xO_7$ samples, almost single zirconolite-2M is observed in the compositional range of $0.1 \leq x \leq 0.9$ while zirconolite-2M (or 3T) is the main phase at $x = 1.0$ with an unknown phase as a trace impurity. Single zirconolite-2M was only observed within the compositional range $0.1 \leq x \leq 0.6$ in the $Ca_{1-x}Yb_xZrTi_{2-x}Fe_xO_7$ solid solutions. When increasing the Yb and Fe contents ($0.7 \leq x \leq 1.0$), additional reflections were detected in the XRD patterns, which cannot be assigned to zirconolite-2M and may relate to the formation of an unknown phase.

In addition, the lattice parameters of zirconolite phase were also calculated from the XRD data with Pawley refinement method. Results show that the lattice parameters change obviously with increasing the dopants concentrations, indicating the incorporation of the lanthanides and Fe in the zirconolite structure. It is also noted that the evolution of lattice parameters of zirconolite-2M among $Ca_{1-x}Ln_xZrTi_{2-x}Fe_xO_7$ (Ln = Nd, Gd, Ho, Yb) solid solutions shows substantial differences. These differences may arise from both of

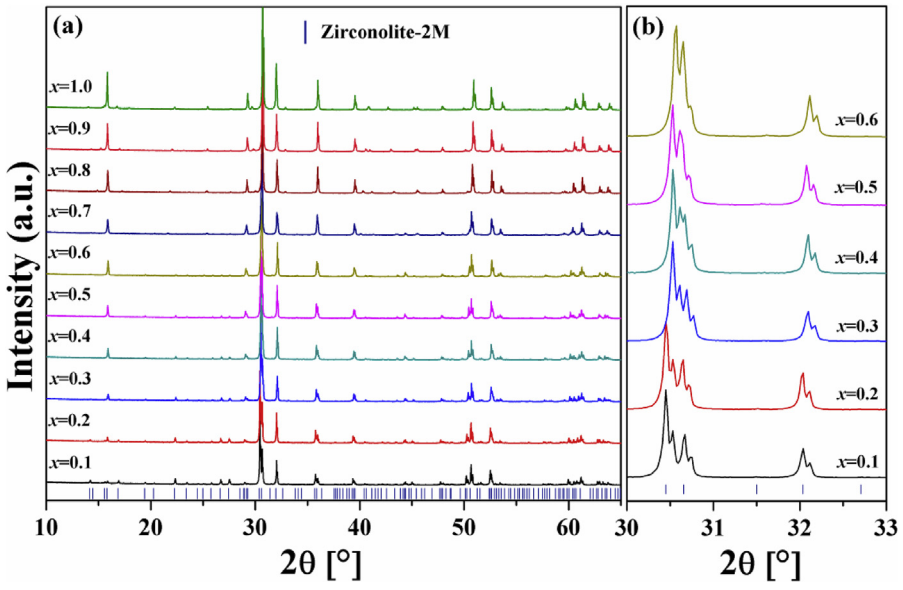

Fig. 10. Representative XRD patterns of $Ca_{1-x}Yb_xZrTi_{2-x}Fe_xO_7$ ($x = 0.1$–1.0) samples (a). Details of XRD patterns among $30° \leq 2\theta \leq 33°$ indicated the peak shifting of zirconolite-2M (b).

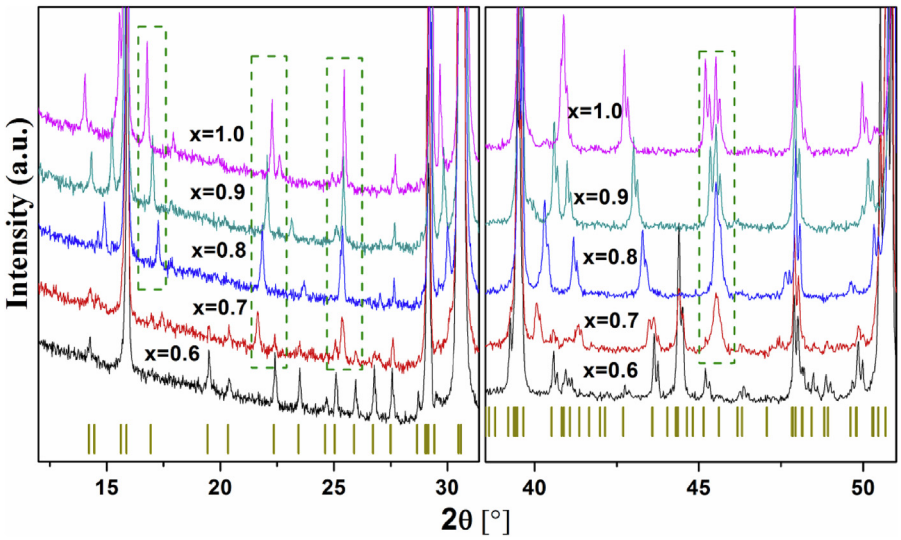

Fig. 11. Detailed XRD patterns of $Ca_{1-x}Yb_xZrTi_{2-x}Fe_xO_7$ ($x = 0.6–1.0$) samples in the ranges of $12° \leq 2\theta \leq 31.4°$ and $38.5° \leq 2\theta \leq 51°$. The rectangles with dotted line indicate the additional reflections.

Table 4
Lattice parameters of zirconolite-2M in $Ca_{1-x}Yb_xZrTi_{2-x}Fe_xO_7$ solid solution.

x	Phase	a(Å)	b(Å)	c(Å)	β(°)
$x = 0.1$	2M	12.451(5)	7.268(3)	11.380(4)	100.55 (1)
$x = 0.2$	2M	12.449(5)	7.257(3)	11.373(2)	100.55(1)
$x = 0.3$	2M	12.452(4)	7.249(3)	11.370(4)	100.54(1)
$x = 0.4$	2M	12.453(1)	7.241(1)	11.363(1)	100.55(1)
$x = 0.5$	2M	12.454(1)	7.235(1)	11.359(1)	100.56(1)
$x = 0.6$	2M	12.455(4)	7.230(2)	11.355(4)	100.58(1)
$x = 0.7$	2M	12.456(13)	7.216(8)	11.354(12)	100.56(2)
$x = 0.8$	2M	12.451(2)	7.195(1)	11.364(2)	100.52(1)
$x = 0.9$	2M	12.424(1)	7.186(1)	11.359(1)	100.51(1)
$x = 1.0$	2M	12.415(2)	7.174(2)	11.381(3)	100.46(1)

the radius difference of cations (Ca^{2+}, Ln^{3+}, Zr^{4+}, Ti^{4+} and Fe^{3+}) and the different substitution mechanisms of Nd, Gd, Ho and Yb in the zirconolite structure.

Acknowledgments

The authors would like to thank Frankie Y. F. Chan from The University of Hong Kong for his help with the SEM experiments. This study was funded by the National Natural Science Foundations of China (41701560, 11475076 and 11775102), the Guangdong Science and Technology Foundation of China (2016B020242006, 2016TX03Z086 and 2017B030314092), the Guangzhou Science and Technology Foundation of China (201804010197 and 201704020200), GDAS' Special Project of Science and Technology Development (2017GDASCX-0834), the Research Grants Council of Hong Kong (Projects 17212015, C7044-14G, and T21-771/16R), the Fundamental Research Funds for the Central Universities (Lanzhou University, No. lzujbky-2018-19).

References

[1] R.C. Ewing, Ceramic matrices for plutonium disposition, Prog. Nucl. Energy 49 (8) (2007) 635–643.
[2] S.V. Yudintsev, S.V. Stefanovsky, R.C. Ewing, Chapter 13-Actinide host phases as radioactive waste forms A2-Krivovichev, Sergey V, in: P.C. Burns, I.G. Tananaev (Eds.), Structural Chemistry of Inorganic Actinide Compounds, Elsevier, Amsterdam, 2007, pp. 457–490.
[3] W.E. Lee, M.I. Ojovan, M.C. Stennett, N.C. Hyatt, Immobilisation of radioactive waste in glasses, glass composite materials and ceramics, Adv. Appl. Ceram. 105 (1) (2006) 3–12.
[4] I. Donald, B. Metcalfe, R.J. Taylor, The immobilization of high level radioactive wastes using ceramics and glasses, J. Mater. Sci. 32 (22) (1997) 5851–5887.
[5] W.J. Weber, A. Navrotsky, S. Stefanovsky, E.R. Vance, E. Vernaz, Materials science of high-level nuclear waste immobilization, MRS Bull. 34 (1) (2009) 46–53.
[6] V.S. Sergey, V.Y. Sergey, Titanates, zirconates, aluminates and ferrites as waste forms for actinide immobilization, Russ. Chem. Rev. 85 (9) (2016) 962.
[7] G.R. Lumpkin, Ceramic waste forms for actinides, Elements 2 (6) (2006) 365–372.
[8] W.J. Weber, R.C. Ewing, C.R.A. Catlow, T.D. de la Rubia, L.W. Hobbs, C. Kinoshita, H. Matzke, A.T. Motta, M. Nastasi, E.K.H. Salje, E.R. Vance, S.J. Zinkle, Radiation effects in crystalline ceramics for the immobilization of high-level nuclear waste and plutonium, J. Mater. Res. 13 (6) (1998) 1434–1484.
[9] R.C. Ewing, Nuclear waste forms for actinides, Proc. Natl. Acad. Sci. U.S.A. 96 (7) (1999) 3432–3439.
[10] P. Pöml, T. Geisler, R.J.M. Konings, High-temperature heat capacity of zirconolite ($CaZrTi_2O_7$), J. Chem. Thermodyn. 38 (8) (2006) 1013–1016.
[11] G.R. Lumpkin, K.L. Smith, R. Gieré, C.T. Williams, Geochemical behaviour of host phases for actinides and fission products in crystalline ceramic nuclear waste forms, Geol. Soc. London, Spec. Pub. 236 (1) (2004) 89–111.
[12] F. Bellatreccia, G. Ventura, C. Terry Williams, G. Lumpkin, K. Smith, M. Colella, Non-metamict zirconolite polytypes from the feldspathoid-bearing alkali-syenitic ejecta of the Vico volcanic complex (Latium, Italy), Eur. J. Mineral 14 (2002) 809–820.
[13] F. Mazzi, R. Munno, Calciobetafite (new mineral of the pyrochlore group) and related minerals from Campi Flegrei, Italy; crystal structures of polymignyte and zirkelite: comparison with pyrochlore and zirconolite, Am. Mineral. 68 (1–2) (1983) 262–276.
[14] N.V. Zubkova, N.V. Chukanov, I.V. Pekov, B. Ternes, W. Schüller, D.A. Ksenofontov, D.Y. Pushcharovsky, The crystal structure of nonmetamict Nb-rich zirconolite-3T from the Eifel paleovolcanic region, Germany, Z. für Kristallogr. - Cryst. Mater. 233 (2018) 463–468.
[15] A.E. Ringwood, S.E. Kesson, N.G. Ware, W. Hibberson, A. Major, Immobilisation of high level nuclear reactor wastes in SYNROC, Nature 278 (1979) 219.
[16] H.J. Rossell, Zirconolite—a fluorite-related superstructure, Nature 283 (1980) 282.
[17] I.E. Grey, W.G. Mumme, T.J. Ness, R.S. Roth, K.L. Smith, Structural relations between weberite and zirconolite polytypes—refinements of doped 3T and 4M $Ca_2Ta_2O_7$ and 3T $CaZrTi_2O_7$, J. Solid State Chem. 174 (2) (2003) 285–295.
[18] A.A. Coelho, R.W. Cheary, K.L. Smith, Analysis and structural determination of Nd-substituted Zirconolite-4M, J. Solid State Chem. 129 (2) (1997) 346–359.
[19] K. Smith, Structural features of zirconolite, hollandite and perovskite, the major wastebearing phases in Synroc, in: Defects and Processes in the Solid State: Gwoscience Applications, 1993, pp. 401–422.
[20] J. Mohsin, S. Pranesh, A.S. N, T.A. K, Phase evolution and microstructural studies in $CaZrTi_2O_7$–$Nd_2Ti_2O_7$ system, J. Am. Ceram. Soc. 97 (2) (2014) 609–616.
[21] M. Jafar, P. Sengupta, S.N. Achary, A.K. Tyagi, Phase evolution and microstructural studies in $CaZrTi_2O_7$ (zirconolite)–$Sm_2Ti_2O_7$ (pyrochlore) system, J. Eur. Ceram. Soc. 34 (16) (2014) 4373–4381.
[22] E.R. Vance, B.D. Begg, R.A. Day, C.J. Ball, Zirconolite-rich ceramics for actinide wastes, MRS Proc. 353 (1994) 767.

[23] P. Loiseau, D. Caurant, N. Baffier, C. Fillet, Structural characterization of polycrystalline (Nd, Al)-substituted zirconolite, MRS Proc. 757 (2002). II6.3.
[24] M.R. Gilbert, C. Selfslag, M. Walter, M.C. Stennett, J. Somers, N.C. Hyatt, F.R. Livens, Synthesis and characterisation of Pu-doped zirconolites–$(Ca_{1-x}Pu_x)Zr(Ti_{2-2x}\ Fe_{2x})O_7$, IOP Conf. Ser. Mater. Sci. Eng. 9 (1) (2010), 012007.
[25] B.D. Begg, E.R. Vance, B.A. Hunter, J.V. Hanna, Zirconolite transformation under reducing conditions, J. Mater. Res. 13 (11) (1998) 3181–3190.
[26] G. Wen, K. Zhang, D. Yin, H. Zhang, Solid-state reaction synthesis and aqueous durability of Ce-doped zirconolite-rich ceramics, J. Nucl. Mater. 466 (2015) 113–119.
[27] B.M. Clark, S.K. Sundaram, S.T. Misture, Polymorphic transitions in cerium-substituted zirconolite ($CaZrTi_2O_7$), Sci. Rep. 7 (1) (2017) 5920.
[28] E.R. Vance, C.J. Ball, R.A. Day, K.L. Smith, M.G. Blackford, B.D. Begg, P.J. Angel, Actinide and rare earth incorporation into zirconolite, J. Alloy. Comp. 213–214 (1994) 406–409.
[29] B.D. Begg, E.R. Vance, R.A. Day, M. Hambley, S.D. Conradson, Plutonium and neptunium incorporation in zirconolite, MRS Proc. 465 (1996) 325.
[30] E.R. Vance, G.R. Lumpkin, M.L. Carter, D.J. Cassidy, C.J. Ball, R.A. Day, et al., Incorporation of uranium in zirconolite ($CaZrTi_2O_7$), J. Am. Ceram. Soc. 85 (7) (2002) 1853–1859.
[31] S.E. Kesson, W.J. Sinclair, A.E. Ringwood, Solid solution limits in synroc zirconolite, Nucl. Chem. Waste Manag. 4 (3) (1983) 259–265.
[32] P. Loiseau, D. Caurant, N. Baffier, L. Mazerolles, C. Fillet, Glass–ceramic nuclear waste forms obtained from SiO_2–Al_2O_3–CaO–ZrO_2–TiO_2 glasses containing lanthanides (Ce, Nd, Eu, Gd, Yb) and actinides (Th): study of internal crystallization, J. Nucl. Mater. 335 (1) (2004) 14–32.
[33] C.Z. Liao, K. Shih, W.E. Lee, Crystal structures of Al–Nd codoped zirconolite derived from glass matrix and powder sintering, Inorg. Chem. 54 (15) (2015) 7353–7361.
[34] X. Cai, Y. Teng, L. Wu, K. Zhang, Y. Huang, The synthesis and chemical durability of Nd-doped single-phase zirconolite solid solutions, J. Nucl. Mater. 479 (2016) 455–460.
[35] M. Jafar, S.N. Achary, N.P. Salke, A.K. Sahu, R. Rao, A.K. Tyagi, X-ray diffraction and Raman spectroscopic investigations on $CaZrTi_2O_7$-$Y_2Ti_2O_7$ system: delineation of phase fields consisting of potential ceramic host materials, J. Nucl. Mater. 475 (2016) 192–199.
[36] G. Pawley, Unit-cell refinement from powder diffraction scans, J. Appl. Crystallogr. 14 (6) (1981) 357–361.
[37] B.H. Toby, R.B. Von Dreele, GSAS-II: the genesis of a modern open-source all purpose crystallography software package, J. Appl. Crystallogr. 46 (2) (2013) 544–549.
[38] M. Vidmar, A. Golobič, A. Meden, D. Suvorov, S.D. Škapin, Sub-solidus phase relations and a structure determination of new phases in the CaO–La_2O_3–TiO_2 system, J. Eur. Ceram. Soc. 35 (10) (2015) 2801–2814.
[39] R. Shannon, Revised effective ionic radii and systematic studies of interatomic distances in halides and chalcogenides, Acta Crystallogr. A 32 (5) (1976) 751–767.